

Simulation of Sheet and Tip Vortex Cavitation on a Rotating Propeller Using a Multiscale Two-Phase Flow Model

Chao-Tsung Hsiao, Jingsen Ma, and Georges L. Chahine

DYNAFLOW, INC.

10621-J Iron Bridge Road, Jessup, MD 20794, USA

ABSTRACT

The flow field of a propeller blade experiencing sheet and tip vortex cavitation is simulated using a multiscale two-phase flow Eulerian/Lagrangian approach which includes a micro-scale model tracking microbubbles, a macro-scale model capturing large cavities and a transition scheme bridges the micro and macro scales. A transition scheme bridges the micro and macro scales. The cavitation patterns on the propeller are compared for three different advance coefficients at the same cavitation number. For the higher advance coefficient the sheet cavity is seen to occur near the blade tip and downstream of the blade mid-chord. As the advance coefficient is reduced, the sheet cavitation extends toward the leading edge. Finally, at the smallest advance coefficient, the tip vortex fills with cavitation bubbles into a well-developed elongated cavity. For all three cases studied the sheet cavity is observed to extend beyond the trailing edge. Under the test conditions simulated no significant sheet cavity oscillations, detachment, and collapse is observed. Instead, small sheet volume oscillations are observed due to shearing off of the cavity near the trailing edge by the wake flow.

Keywords

Propeller, Cavitation, Sheet, Tip Vortex, Two-Phase Flow, Multiscale

1 INTRODUCTION

Different forms of cavitation, such as traveling bubble cavitation, tip vortex cavitation, sheet cavitation, cloud cavitation, and supercavitation can appear on a propeller depending on its operating conditions. A general numerical model to accurately capture all these cavitation forms is highly desirable, especially that several of these forms can coexist under some operating conditions. However, this task is not simple, as these various forms involve many length and time scales and complex features such as: presence of bubbles, nucleation, bubbly flow, bubble

coalescence and breakup, turbulence, presence of vortical structures, deforming and moving free surfaces, free surface instability and break-up, .. etc. In addition, several aspects of the physics are not fully understood despite many experimental studies (Arndt, 1981; Arndt, 2002; Rood, 1991).

Several numerical methods have been developed for modeling sheet and sheet-to-cloud cavitation. Conventionally most approaches identify and track as the sheet interface the region where the pressure drops below the vapor pressure. The liquid phase flow can be solved either by a Navier-Stokes solver (Chen & Heister, 1994; Deshpande, Feng, & Merkle, 1993; Hirschi, Dupont, & Avellan, 1998) or a potential flow solver using a boundary element method (G L Chahine & Hsiao, 2000; Kinnas & Fine, 1993; Varghese, Uhlman, & Kirschner, 2005).

Since the sheet cavity of interest here can be very unsteady and highly dynamic, methods needing a moving grid to resolve the flow field are accurate but encounter numerical difficulties to describe folding or breaking up of the interfaces. Approaches have thus been developed to avoid using moving grids to track the liquid-gas interface. They can be subdivided into two categories: Volume of Fluid methods (VoF) (Kunz et al., 2000; Merkle, Feng, & Buelow, 1998; Singhal, Athavale, Li, & Jiang, 2002; Yuan, Sauer, & Schnerr, 2001) and Level-Set Methods (LSM) (Dabiri, Sirignano, & Joseph, 2007, 2008; Kawamura & Sakoda, 2003; Kinzel, Lindau, & Kunz, 2009). While both interface capturing methods solve a Navier-Stokes equation using a fixed computational grid, liquid/gas interfaces are captured differently. In the VoF method, an advection equation for the vapor volume fraction is solved and the density is computed locally using this according to the volume fraction. This method does not use sharp interfaces where boundary conditions are imposed, however it requires a mass transfer model, often using fitting factors to match experimental results. In the LS method, the interface is sharp and its location is determined by solving an advection equation for a level set function with the interface

being the iso-surface of level zero. On this interface boundary conditions are imposed as in interface tracking schemes, i.e. a constant pressure and zero shear stress.

Interface capturing approaches have been successful at solving the dynamic evolution of sheet cavities but are not appropriate for dispersed bubbles and their transition to the sheet since to resolve the small bubbles a much finer spatial resolution of the domain is required (Fedkiw, Aslam, Merriman, & Osher, 1999; Osher & Fedkiw, 2001). Resolving the small bubbles and with the sheet cavity would require grids several orders of magnitude smaller than the grid resolution affordable to the best computational resources currently available.

To overcome these numerical challenges and model traveling bubbles, sheet and cloud cavitation, Hsiao et al. (2014) developed a multiscale two-phase flow model which combines a macro-scale model for simulation of sheet cavity, a micro-scale model for tracking small nuclei, and a meso-scale model to smoothly bridge the micro and macro scales. In addition, this model addressed the inception mechanisms of sheet cavitation as it demonstrated its prediction capabilities using exclusively free field nuclei and nucleation from the boundaries without requiring any mass exchange model to simulate unsteady sheet cavitation. The model has been demonstrated to reproduce accurately lengths and oscillation frequencies when compared with experimental results (Berntsen, Kjeldsen, & Arndt, 2001). In this study we will further extend this model to simulate various form of cavitation on a rotating propeller.

2 MULTISCALE TWO-PHASE FLOW MODEL

The sketch in Figure 1 presents an overview of the multi-scale model used in this study. The model addresses the physics at the various scales as follows:

- At the micro-scale, transport of nuclei and microbubbles, nucleation from solid surfaces, and corresponding bubble dynamics are considered. The model uses a Discrete Singularity Model (DSM) to handle dispersed pre-existing nuclei in the liquid, nuclei originating from the solid boundaries, and micro-bubbles resulting from disintegration of sheet and cloud cavities or bubbles breaking up from vaporous/gaseous cavities. At this scale, the model tracks the bubbles in a Lagrangian fashion.
- At the macro-scale, a two-phase continuum-based flow is solved on an Eulerian grid. At this scale gas/liquid interfaces of large bubbles, air pockets, and cavities are directly discretized and resolved through tracking the gas-liquid interfaces with a Level Set method.
- Inter-scale transition schemes are used to bridge micro and macro scales as bubbles grow or merge to form large cavities, or as bubbles shrink or break up from a large cavity. At this scale, model transition between micro-scale and macro-scale and vice-versa is realized

by using information from both the Discrete Singularity Model (DSM) and the Level Set method (LSM).

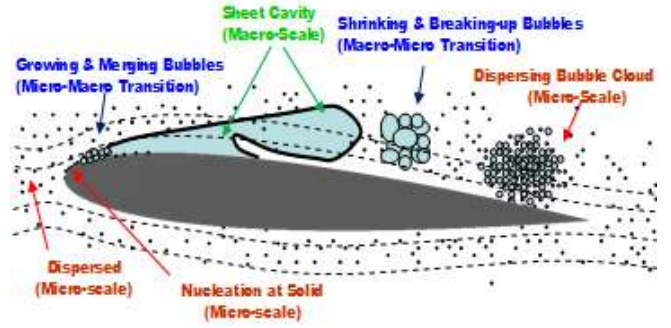


Figure 1: Overview of the various scales in the problem of cavitation on a blade and sketch of the modeling strategy.

2.1 Eulerian Continuum Flow Model

The two-phase medium continuum model uses the viscous flow solver, 3DYNAPS-VIS[®], to solve the Navier-Stokes equations and satisfy the two-phase continuity and momentum equations:

$$\frac{\partial \rho_m}{\partial t} + \nabla \cdot (\rho_m \mathbf{u}) = 0,$$

$$\rho_m \frac{D\mathbf{u}}{Dt} = -\nabla p + \nabla \cdot \left\{ \mu_m \left(\frac{\partial u_i}{\partial x_j} + \frac{\partial u_j}{\partial x_i} \right), -\frac{2}{3} \mu_m (\nabla \cdot \mathbf{u}) \delta_{ij} \right\}, \quad (0)$$

where the subscript m represents the mixture properties, \mathbf{u} is the mixture velocity, p is the pressure, and δ_{ij} is the Kronecker delta. The mixture density, ρ_m , and the mixture viscosity, μ_m , can be expressed as functions of the void volume fraction α :

$$\rho_m = (1-\alpha)\rho_l + \alpha\rho_g, \quad \mu_m = (1-\alpha)\mu_l + \alpha\mu_g, \quad (0)$$

where the subscript l represents the liquid and the subscript g represents the gas.

The equivalent continuum has a time and space dependent density since the void fraction α varies in both space and time. This makes the overall flow field problem similar to a compressible flow problem. In our approach, which couples the continuum medium with the discrete bubbles, the mixture density is not an explicit function of the pressure through an equation of state. Instead, tracking the bubbles and knowing their concentration provides α and ρ_m as functions of space and time. This is achieved by using a Gaussian distribution scheme which smoothly “spreads” each bubble’s volume over a selected spherical radius over the discretization cell and the neighboring cells while conserving the total bubble volumes (Ma, Chahine, & Hsiao, 2015). Specifically, for a fluid cell i , the void fraction in it is computed by:

$$\alpha_i = \sum_{j=1}^{N_i} \frac{f_{i,j} V_j^b}{\sum_k^{N_{cells}} f_{k,j} V_k^{cell}}, \quad (1)$$

where V_j^b and V_k^{cell} are the volumes of a bubble j and cell k respectively, N_i is the number of bubbles which are influencing cell i . N_{cells} is the total number of cells “influenced” by a bubble j . $f_{i,j}$ is the weight of the contribution of bubble j to cell i and is determined by the Gaussian distribution function. This scheme has been found to significantly increase numerical stability and to enable the handling of high-void bubbly flow simulations.

The system of equations is closed by an artificial compressibility method (Chorin, 1967) in which a pseudo-time derivative of the pressure multiplied by an artificial-compressibility factor, β , is added to the continuity equation as

$$\frac{1}{\beta} \frac{\partial p}{\partial \tau} + \frac{\partial \rho_m}{\partial t} + \nabla \cdot (\rho_m \mathbf{u}) = 0 \quad (2)$$

As a consequence, a hyperbolic system of equations is formed and can be solved using a time marching scheme. This method can be marched in pseudo-time to reach a steady-state solution. To obtain a time-dependent solution, a Newton iterative procedure is performed at each physical time step in order to satisfy the continuity equation.

3DYNAFS-VIS[®] uses a finite volume formulation. First-order Euler implicit differencing is applied to the time derivatives. The spatial differencing of the convective terms uses the flux-difference splitting scheme based on Roe’s method (Roe, 1981) and van Leer’s MUSCL method (van Leer & Woodward, 1979) for obtaining the first-order and the third-order fluxes, respectively. A second-order central differencing is used for the viscous terms which are simplified using the thin-layer approximation. The flux Jacobians required in an implicit scheme are obtained numerically. The resulting system of algebraic equations is solved using the Discretized Newton Relaxation method (Vanden & Whitfield, 1995) in which symmetric block Gauss-Seidel sub-iterations are performed before the solution is updated at each Newton iteration.

2.2 Level-Set Approach

In order to enable 3DYNAFS-VIS[®] to simulate large free surface deformations including folding and breakup as in a sheet cavity, a Level-Set method is used. A smooth function $\varphi(x, y, z, t)$, whose zero level coincides with the liquid/gas interface when the level set is introduced, is defined in the whole physical domain (i.e. in both liquid and gas phases) as the signed distance $d(x, y, z)$ from the interface:

$$\varphi(x, y, z, 0) = d(x, y, z). \quad (3)$$

This function is enforced to be a material surface at each time step using:

$$\frac{d\varphi}{dt} = \frac{\partial \varphi}{\partial t} + \mathbf{v}_j \cdot \frac{\partial \varphi}{\partial \mathbf{x}_j} = 0, \quad (4)$$

where \mathbf{v} is the velocity of interface. Integration of Equation (4) does not ensure that $\varphi(x, y, z, t)$ remains at all times the correct distance function for all grid points during the computations due to numerical diffusion and to distortion by the flow field. To avoid this problem, a new distance function $\tilde{\varphi}$ is constructed by solving a “re-initialization equation” with $\varphi(x, y, z, t)$ as the initial solution (Sussman, Smereka, & Osher, 1998):

$$\frac{\partial \tilde{\varphi}}{\partial \tau} = S(\varphi) [1 - |\nabla \tilde{\varphi}|], \quad (5)$$

where τ is the pseudo time, $S(\varphi)$ is a sign function based on the value of $\varphi(x, y, z, t)$. Equation (5) is solved during the pseudo iteration until $\partial \tilde{\varphi} / \partial \tau$ approaches zero and thus recovers the correct distance function as $|\nabla \tilde{\varphi}| = 1$ since φ is nothing but the distance measured along the normal to the surface its normal derivative is unity.

In a standard Level-Set approach liquid and gas phases are solved separately using Equations (4) and (5) after identifying to which phase a concerned cell belongs and applying a smoothed Heaviside function over the interface to smooth the fluid properties. Here, instead of solving both phases, a single phase level-set method using the Ghost Fluid Method (Fedkiw et al., 1999; Kang, Fedkiw, & Liu, 2000) enables to maintain a sharper interface. This method allows imposing the dynamics boundary conditions at the interface without using smoothing functions. The shear due to gas/vapor is neglected and the dynamic boundary conditions (balance of normal stresses and zero shear) are as follows:

$$p = \frac{\tau_{ij} n_i n_j}{\rho_l} + \frac{gz}{\rho_l} + \frac{\gamma \kappa}{\rho_l}, \quad \tau_{ij} n_i t_j^1 = 0, \quad \tau_{ij} n_i t_j^2 = 0. \quad (6)$$

where τ_{ij} is the stress tensor, g is the acceleration of gravity, and γ is the surface tension. $\kappa = \nabla \cdot \nabla \varphi / |\nabla \varphi|$ is the surface curvature. \bar{n} , \bar{t}^1 , and \bar{t}^2 are the normal to the surface and two tangential unit vectors, respectively.

In this approach one or more ghost cells are used at the interface to impose the boundary conditions. The interface cells for each phase are identified when one of the following six inequalities is satisfied for two adjacent cells:

$$\begin{aligned} \varphi_{i,j,k} \varphi_{i\pm 1,j,k} &< 0, \\ \varphi_{i,j,k} \varphi_{i,j\pm 1,k} &< 0, \\ \varphi_{i,j,k} \varphi_{i,j,k\pm 1} &< 0. \end{aligned} \quad (7)$$

To apply the single-phase level-set approach the cells belonging to the gas phase are deactivated during the computations. To solve Equation (4), we impose the following condition across the interface:

$$\mathbf{n}\nabla u_i = 0, \quad \mathbf{n} = \nabla\phi/|\nabla\phi|, \quad (8)$$

which means there is no normal component of the velocity gradient at the interface. With this assumption we can extend the velocity from the liquid phase to the gas phase along the interface normal by solving the pseudo time iteration equation:

$$\frac{\partial u_i}{\partial \tau} + \mathbf{n} \cdot \nabla u_i = 0. \quad (9)$$

2.3 Lagrangian Discrete Bubble Model

The Lagrangian discrete bubble model is based on DYNAFLOW's discrete singularity model, 3DYNAFS-DSM[®], which uses a Surface Average Pressure (SAP) approach to average fluid quantities along the bubble surface (Chahine, 2009; Choi et al., 2004; Hsiao et al., 2003). This model has been shown to produce accurate results when compared to full 3D two-way interaction computations (Hsiao & Chahine, 2004) The averaging scheme allows one to consider only a spherical equivalent bubble and use the following modified Rayleigh-Plesset equation (Hsiao et al., 2003) to describe the bubble dynamics,

$$R\ddot{R} + \frac{3}{2}\dot{R}^2 = \frac{1}{\rho_l} \left(p_v + p_{g0} \left(\frac{R_0}{R} \right)^{3K} - p_{enc} - \frac{2\gamma}{R} - \frac{4\mu\dot{R}}{R} \right) + \frac{|\mathbf{u}_s|^2}{4}, \quad (10)$$

where $\mathbf{u}_s = \mathbf{u}_{enc} - \mathbf{u}_b$, R and R_0 are the bubble radii at time t and 0, p_v is the liquid vapor pressure, p_{g0} is the initial bubble gas pressure, K is the polytropic compression constant, \mathbf{u}_b is the bubble travel velocity, while \mathbf{u}_{enc} and p_{enc} are respectively the liquid velocity and the ambient pressure "seen" by the bubble during its travel. With the SAP model, \mathbf{u}_{enc} and p_{enc} are respectively the averages of the liquid velocities and of the pressures over the bubble surface.

The bubble trajectory is obtained from the following bubble motion equation:

$$\frac{d\mathbf{u}_b}{dt} = \left(\frac{\rho_l}{\rho_b} \right) \left[\frac{3}{8R} C_D |\mathbf{u}_s| \mathbf{u}_s + \frac{1}{2} \left(\frac{d\mathbf{u}_{enc}}{dt} - \frac{d\mathbf{u}_b}{dt} \right) + \frac{3\dot{R}}{2R} \mathbf{u}_s - \frac{\nabla p}{\rho_l} + \frac{(\rho_b - \rho_l)}{\rho_l} g + \frac{3C_L}{4\pi R} \frac{\sqrt{v}}{\sqrt{|\Omega|}} \mathbf{u}_s \times \Omega \right], \quad (11)$$

where ρ_b is the bubble content density, C_D is the drag coefficient given by an empirical equation such as from Haberman and Morton (1953), C_L is the lift coefficient and Ω is the deformation tensor. The 1st right hand side term is a drag force. The 2nd and 3rd terms account for the added mass. The 4th term accounts for the presence of a pressure gradient, while the 5th term accounts for gravity and the 6th term is a lift force (Saffman, 1965).

2.4 Transition Model between Micro- and Macro-Scale

The transformation from micro- to macro-scale and vice-versa includes two scenarios illustrated in Figure 3:

- transition from microbubbles into a large discretized non-spherical deformable cavity,
- transition from a large cavity into a set of microscopic dispersed bubbles,

In the first scenario, since the bubbles are tracked using the Lagrangian scheme, the bubble sizes and locations are known at every time step. A criterion based on bubble size is set to "activate" the bubbles for computation of a local distance function for neighboring cells. For each cell i , the distance function is then defined by:

$$\varphi_i = \min(\varphi_{LS0}, \varphi_{b,j}); \quad j = 1, N_i, \quad (12)$$

where φ_{LS0} is the original distance function value for cell i , $\varphi_{b,j}$ is the local distance between the center of cell i and the surface of bubble j as shown in Figure 2, and N_i is the number of bubbles which are "activated" around cell i . This scheme allows multiple bubbles to merge together into a large cavity, as well as a single bubble to be absorbed by a large cavity. The criterion to determine which bubble to "activate" is as follows:

$$R_b \geq \max(R_{thr}, m_{thr} \Delta L), \quad (13)$$

where R_b is the bubble radius, ΔL is the size of local grid which hosts the bubble, R_{thr} is a threshold bubble radius, and m_{thr} is a threshold multiplier of the local grid size. This indicates that a bubble-singularity becomes a discretized bubble represented by a zero value level set only when it grows beyond a threshold bubble radius and its radius exceed a selected number of local grids. The latter ensures enough grid resolution to define properly the bubble volume.

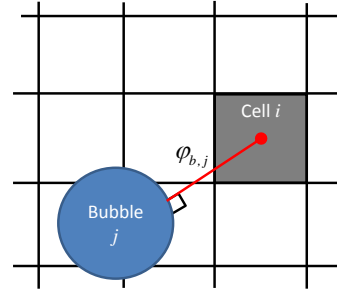


Figure 2: Definition of the local distance $\varphi_{b,j}$.

The second scenario is applied when the volume of a large cavity is decreasing in time. As the cavity collapses, the lost volume is replaced with a distribution of micro-bubbles of the same volume when the continuum normal speed is larger than the interface normal speed.

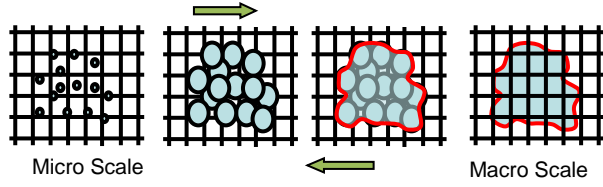


Figure 3: Illustration of the transition between macro- and micro-scale modeling and vice-versa.

2.5 Nucleation Model

A very important aspect of our approach is to account for nucleation from the rigid boundaries in addition to bubble nuclei dispersed in the liquid. The boundary nucleation is easily observed in conditions where gas diffusion (i.e. carbonated drinks) and/or boiling are dominant; bubbles grow out of boundary nucleation spots. This phenomenon has been studied extensively. Harvey et al. (1944) suggested that gas pockets, trapped in hydrophobic conical cracks and crevices of solid surfaces, act as cavitation nuclei. More recently Mørch (2009) investigated further this effect and suggested that a skin model similar to that proposed by Yount (1979) for dispersed nuclei can also be used to describe the wall gas nuclei because solid surfaces submerged in a liquid tend to absorb amphiphilic molecules (molecules having a polar water-soluble group attached to a nonpolar water-insoluble hydrocarbon chain) and capture nanoscopic air pockets. One can expect that clusters of such molecules form weak spots, which are the basis for bubble nucleation from the solid surface when low pressure conditions are achieved. Briggs (2004), for instance, found that scrupulous cleanliness was decisive for obtaining a high tensile strength of water, and that contamination of interfaces is a primary factor in cavitation. Atchley & Prosperetti (1989) modeled nucleation out of crevices when the liquid pressure drops and related the threshold pressure to crevice aperture, surface tension, and gas concentration etc.

Our wall nucleation modeling involves the following parameters, which are functions of the wall material properties and its finish and of the local flow conditions:

- P_{thr} : a nucleation pressure threshold,
- N_s : a number density of nucleation sites per unit area,
- f_n : a nucleation rate,
- R_0 : initial nuclei size(s).

With this nucleation model at each time step the pressure at each cell center is obtained from the continuum flow solver and is used to compare with P_{thr} to determine if nucleation should occur. Once the pressure drops below the threshold, the cell releases during the integration time step, Δt , a total of N nuclei given by:

$$N = N_s f_n \Delta t \Delta A, \quad (14)$$

where ΔA is the surface area of the grid cell. Since the Lagrangian solver (bubble tracking) requires much smaller time steps than the Eulerian flow solver, the N nuclei are released randomly in space from the area ΔA , and in time during the time step. All above parameters are presumably functions of surface roughness, temperature, and other physical parameters neglected.

3. COMPUTATIONAL DOMAIN AND PROPELLER GRID

The multiscale model performance is tested on the NSWCCD three-bladed open propeller 5530 (Forero, 2010), which has a diameter $D = 0.4$ m and is illustrated in Figure 3. To simulate the propeller flow in a rotational frame, a one-blade-to-blade passage computational domain which follows the incoming flow angle and forms a spiral shape as shown in Figure 4 is used. The selected computational domain has the inflow boundary located at $R_p = D/2$ and the outflow at $3R_p$ from the propeller mid-plane. The radial domain boundary is located at $2R_p$ from the hub center. Free stream boundary conditions are imposed at inflow, outflow and radial domain boundaries while the two side (blade-to-blade) boundaries have periodic boundary conditions except at the blade surface where no-slip conditions are imposed.

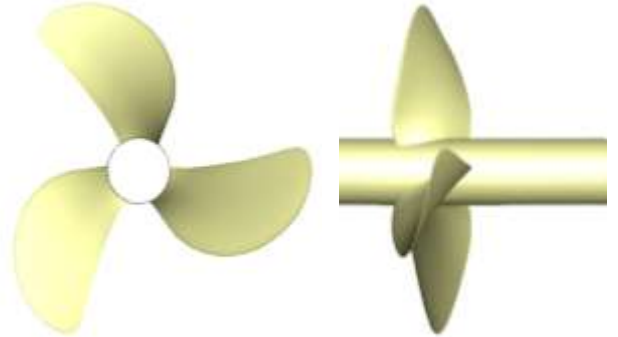


Figure 3: Geometry of the NSWCCD open propeller 5530.

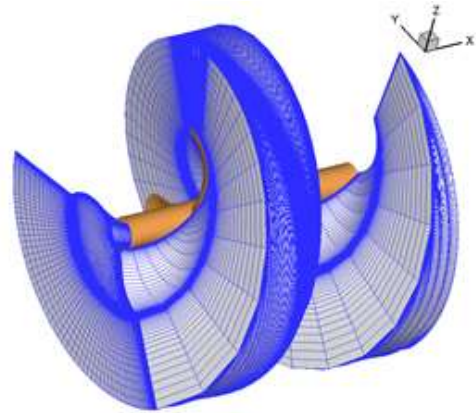


Figure 4: H-H type grid generated for one blade-to-blade passage of the propeller. A total of 2.1 million grid points for the single passage is used in the calculations.

An H-H type grid with 2.1 million grid points is used to generate the grid for the blade-to-blade computational domain. There are 101 grid points from the blade leading edge to the trailing edge and 81 grid points from the root section to the tip section. Care is taken to ensure that grid points closest to the rigid boundary are at distances of $y^+ \sim 3$ from the blade surface to properly capture the boundary layer.

4. SINGLE PHASE FLOW RESULTS

Single-phase flow field simulations of the propeller flow field are obtained using the same model with cavitation modeling turned off. Three sets of computations are shown below for three values of the advance coefficient,

$$J = \frac{U_\infty}{nD}, \quad (15)$$

where n is the number of propeller revolution per unit time, and U_∞ is the free stream velocity. For all three cases U_∞ is kept at 13.89 m/s while three values of n are considered and result in three different Reynolds numbers according to

$$\text{Re} = \frac{\sqrt{U_\infty^2 + (0.7\pi nD)^2} \cdot C_{0.7Rp}}{\nu}, \quad (16)$$

where $C_{0.7Rp} = 0.163$ m is the propeller blade chord length at the 0.7 radius section and ν is the kinematic viscosity.

Table 1 summarizes the characteristics of the three cases studied with $J = 1.0$ being the design condition for Prop5530.

J	0.9	1.0	1.1
U_∞ , m/s	13.89	13.89	13.89
n , s^{-1}	38.07	34.26	31.15
Re	7.41×10^6	6.78×10^6	6.28×10^6

Table 1: Characteristics of the three flow conditions.

The resulting pressure distributions for these three cases are shown in Figure 5 which presents contours of the pressure coefficient, $C_p = (p - P_\infty) / (0.5\rho U_\infty^2)$, on the suction-side surface of the propeller blades and in a plane perpendicular to the propeller axis right behind the propeller blade.

The contours for the flow conditions show that the low pressure region covers the mid-chord region of the blade for higher J and moves toward the leading edge as J increases. This indicates that different cavitation patterns occur in each case.

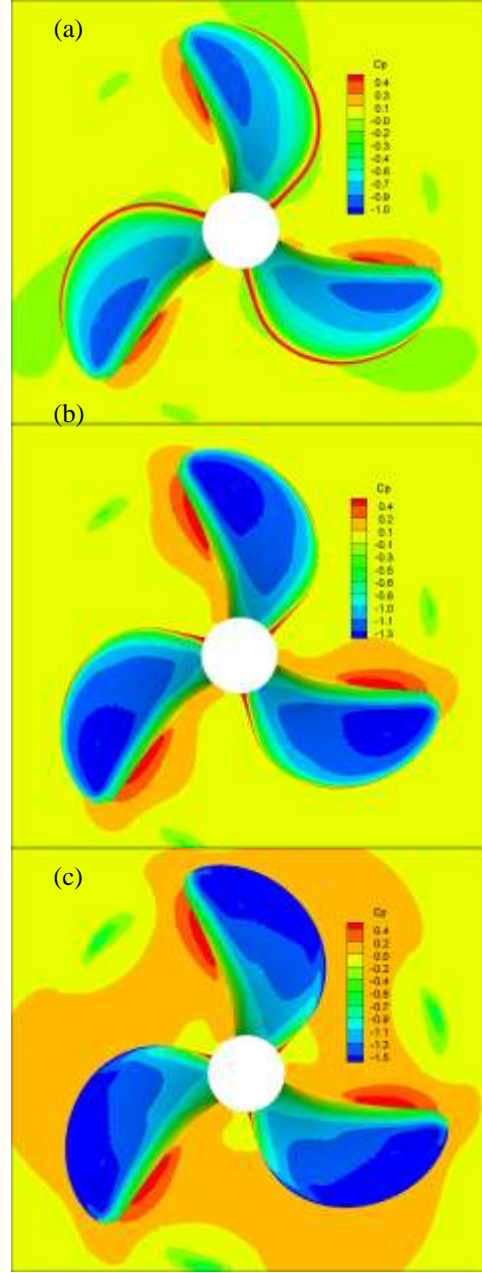


Figure 5: Pressure coefficient, C_p , contours on the suction-side surfaces of the NSWCCD 5530 propeller blades and on a plane perpendicular to the propeller axis right behind the propeller tip trailing edge. a) $J = 1.1$ b) $J = 1.0$ c) $J = 0.9$.

Quantitative comparisons of the pressure distributions along the $r/R_p = 0.85$ strip (r is the radial distance from the hub center) are shown in Figure 6. It is seen that $-C_p$ curve near the leading edge does not have a high peak at the suction side. Even for the $J = 0.9$ case, only a moderate peak is observed.

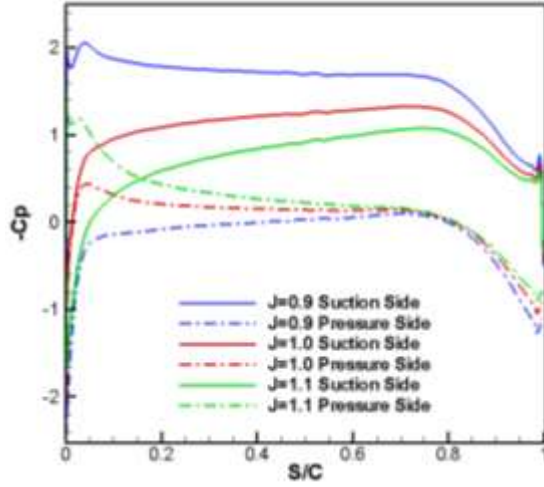


Figure 6: Comparisons of the pressure coefficient distributions along the $r/R_p = 0.85$ blade strip for three difference advance coefficients studied. S is the distance from the leading and C is the chord length $r/R_p = 0.85$ strip.

The computed thrust coefficient, K_t , and torque coefficient, K_q , of the 5530 propeller are compared below in Table 2 with the experimental data measured in an open water test. K_t and K_q are defined as:

$$K_t = \frac{T}{\rho n^2 D^4}, \quad K_q = \frac{Q}{\rho n^2 D^5}, \quad (17)$$

where T and Q are the thrust and torque acting on the propeller. The comparison is very good for the grid used.

J	Comp. K_t	Exp. K_t	Comp. $10K_q$	Exp. $10K_q$
0.9	0.156	0.152	0.308	0.286
1.0	0.113	0.116	0.246	0.233
1.1	0.069	0.080	0.175	0.175

Table 2: Comparison of K_t and K_q for three advance coefficients, J .

5. CAVITATING FLOW SIMULATIONS

The simulation of cavitation on the propeller is started after the single phase flow solution reaches limit cycle oscillation. Water with nuclei is introduced in the domain from upstream and is also released from the surface of foil using the solid surface nucleation model. The field nuclei are selected with sizes ranging from $10 \mu\text{m}$ to $50 \mu\text{m}$ and are distributed randomly in the incoming flow field resulting in a void fraction of 1×10^{-6} . Nucleation from the solid wall is realized with nuclei at size $10 \mu\text{m}$ released initially from the propeller surface when the local pressure drops below vapor pressure according to Equation (14). Here, based on the study by (Hsiao et al. 2014) the number of nucleation sites per unit area, N_s , is selected to be $70/\text{cm}^2$ and the nucleation

frequency rate, f_n , is selected to be 10 kHz. These parameters were chosen to minimize the number of nuclei to be tracked in the Lagrangian model without affecting the modeling of the sheet cavitation according to our previous parametric study on a 2D hydrofoil case (Hsiao et al., 2014).

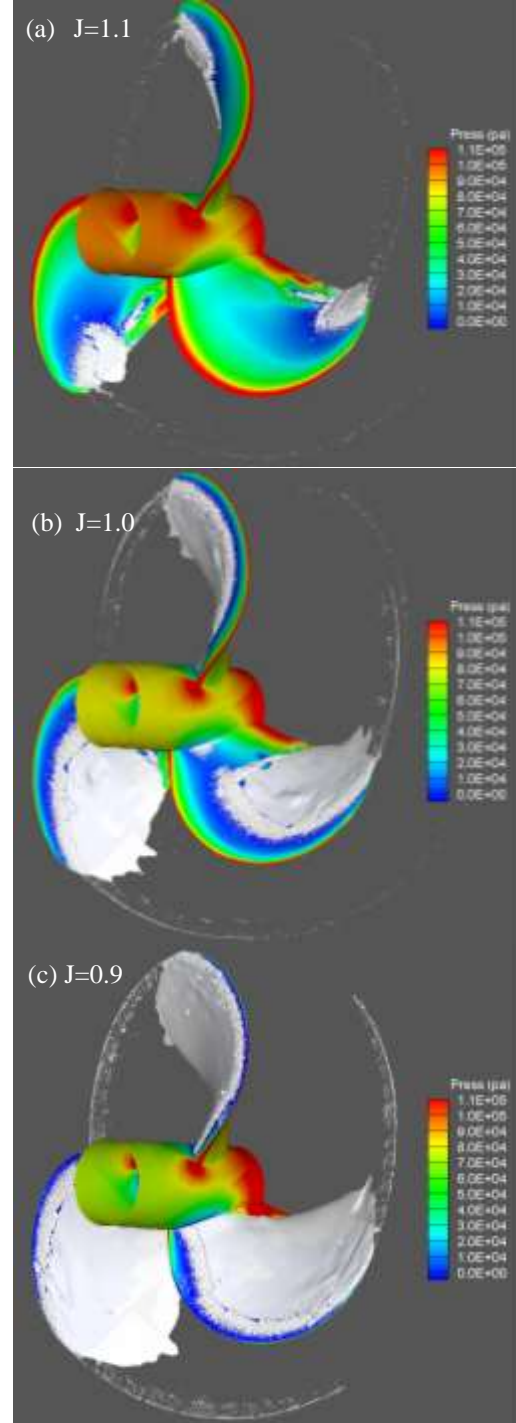


Figure 7: Snapshots showing sheet cavitation and tip vortex cavitation for a) $J = 1.1$, b) $J = 1.0$, and c) $J = 0.9$ at the cavitation number $\sigma = 1.0$.

Concerning multiscale modeling, the singularity microbubbles are switched into a discretized Level Set free surface when their radius exceeds the local grid size and is larger than 700 μm which is about 20 times an initial median nucleus radius.

The simulations for the three above values of the advance coefficient are conducted at a cavitation number $\sigma = (P_\infty - p_v) / (0.5 \rho U_\infty^2) = 1$. This cavitation number is chosen to allow cavitation to occur on the blade surface even for the highest pressure coefficient case, $J = 1.1$, as shown in the pressure distributions in Figure 6. For each case, the simulations were continued until three rotations were completed by the blade. Sheet cavitation and tip vortex cavitation develop gradually from the field nuclei and from nucleation on the blade surface.

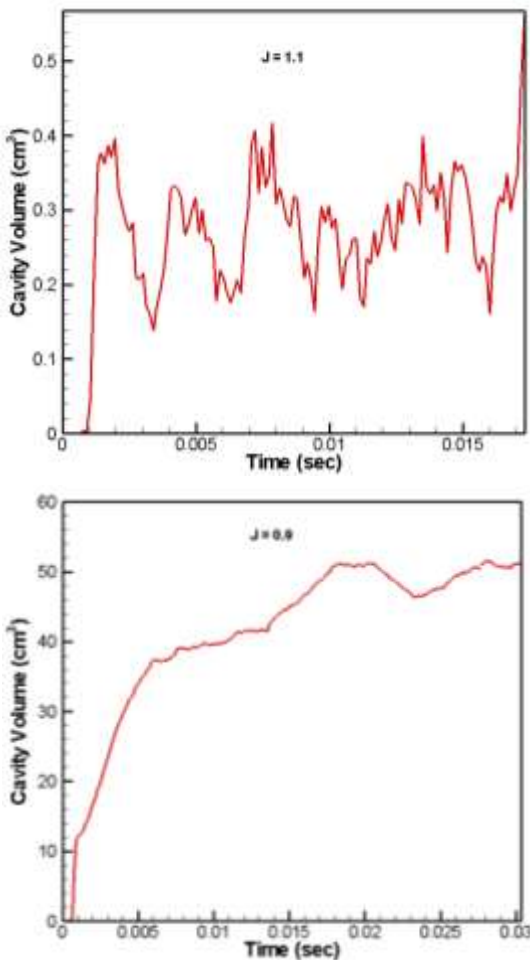


Figure 8: Sheet cavity volume versus time for $J = 1.1$ and 0.9 at cavitation number $\sigma = 1.0$.

Error! Reference source not found. shows snapshot images of the sheet cavity at its maximum extent and the cavitating tip vortex for the three advance coefficients at $\sigma = 1$. It is seen that the sheet cavity extends beyond the trailing edge for all three cases studied. For the $J = 1.1$ case the loading is low and the cavitation only occurs near

the tip and downstream of the mid-chord of the blade. The circulation in tip vortex is not high enough and trapped bubbles in the viscous core do not grow significantly. As J is reduced, the loading increases and the sheet cavitation extends and moves toward the leading edge; the sheet covers almost the full blade surface for $J = 0.9$. In addition, a well-developed tip vortex forms with cavitation bubbles in it and around it for $J = 1.0$ and $J = 0.9$.

In these simulations significant sheet cavity oscillations and breakup into cloud cavitation due to a reentrant jet as in the case of the 2D foil (Hsiao et al., 2014) is not observed. Instead, the volume of sheet cavity is seen to vary in time because the cavity is sheared off by the wake flow near the trailing edge. The volume of the cavity versus time can be seen in Figure 8. It is seen that cavity volume oscillates with large amplitude and high frequency for $J = 1.1$ and lower amplitude and a low frequency for $J = 0.9$. However, longer simulations are needed for better stabilization of the solution.

5.1 Effect of Cavitation on Pressure distribution

It is interesting to examine how cavitation on the blade modifies the pressure distribution shown in Figure 6. The pressure coefficients in the cavitation cases are deduced from time-averaged solutions of the unsteady cavitation flows simulations. Figure 9 compares the pressure distributions along the $r/R_p = 0.85$ blade strip between the single phase and the cavitation conditions at $\sigma = 1.0$ for the three advance coefficients. For $J = 1.1$, the pressure distribution is not significantly modified at this location on both the suction side and pressure side except near the trailing edge where the sheet cavity presents. As J is reduced, the area covered by the sheet cavity increases and modifications of the pressure distribution becomes pronounced. The figure shows that for the area covered by the sheet cavity the pressure coefficient becomes -1.0 , i.e. the pressure is equal to the vapor pressure. Since the area between the pressure and suction curves represents the lift force, one can see that a significant reduction in lift occurs as the cavitation covers almost the whole blade surface for $J = 0.9$ because the pressure is even more reduced on the pressure side.

The present method enables to explain the initiation of the sheet cavity. Unlike other approaches which depict the inception of the sheet cavity where the local pressure drops below the vapor pressure, the current model relies on the growth of the nuclei from the blade surface nucleation or from the incoming flow field. These form the sheet cavity once they grow large enough and collect into a surface cavity. These nuclei behave as traveling bubbles before they merge into a continuous sheet cavity.

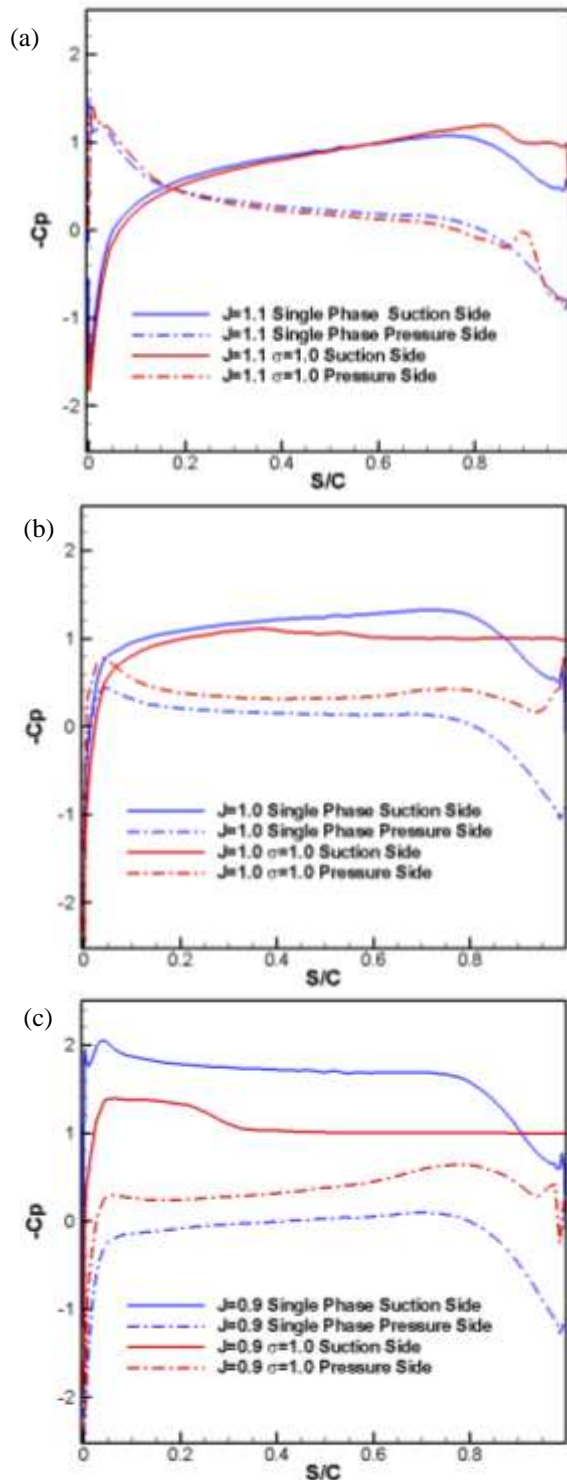


Figure 9: Comparisons of the pressure distributions along the $r/R_p = 0.85$ blade strip between the single phase solution and the cavitation conditions at cavitation $\sigma = 1.0$ and a) $J = 1.1$, b) $J = 1.0$, and c) $J = 0.9$.

The local pressure is modified by the presence of these bubbles. Since there a time laps for these bubbles to grow

while traveling before they become a sheet cavity, a region where the pressure is lower than the vapor pressure could develop before the initiation of the sheet cavity. This buffer zone can be clearly identified on the suction side curves for all three cavitation flow cases shown in Figure 9, where $-C_p$ remains above 1.0 for some distance before it drops to 1.0 where the sheet cavity starts.

6 CONCLUSIONS

A multiscale two-phase flow model based on an Eulerian/Lagrangian approach is applied to simulate the various forms of cavitation on a rotating propeller including sheet and tip vortex cavitation. Starting with free field nuclei and nucleation from solid surfaces traveling bubble, sheet, and tip vortex cavitation can be captured without the need of a mass transfer model and fitting coefficients.

The cavitation flows on the NSWCCD 5530 propeller are compared for three advance coefficients and the same cavitation number. At high J the loading is low and cavitation only occurs near the tip and downstream of the mid-chord of the blade but the circulation in the tip vortex is not high enough for bubbles to grow significantly in the core. As J is reduced, the sheet cavitation extent increases and it moves toward the leading edge. Also, a well-developed tip vortex is seen to fill with bubbles.

For all cases studied the sheet cavitation is observed to extend beyond the blade trailing edge. The volume of the sheet cavity oscillates in time due to the cavity being sheared off periodically near the trailing edge by the wake flow. Significant sheet cavity breakup into clouds due to a reentrant jet is not observed for all three cases studied.

Comparisons of the pressure distributions on the blade surface between the single phase and the cavitating flows show that a significant reduction in lift occurs when the sheet cavity covers a large area of the blade surface as this results in significant modifications of the pressure distribution on both pressure and suction sides of the blade. A buffer zone where the pressure is lower than the vapor pressure is observed upstream of the initiation area of the sheet cavity.

ACKNOWLEDGMENTS

This work was supported by the Office of Naval Research under contract N00014-12-C-0382 monitored by Dr. Ki-Han Kim. This support is highly appreciated.

REFERENCES

- Arndt, R. E. A. (1981). Cavitation in Fluid Machinery and Hydraulic Structures. *Annual Review of Fluid Mechanics*, 13(1), 273–326.
- Arndt, R. E. A. (2002). Cavitation in vortical flows. *Annual Review of Fluid Mechanics*, 34(1), 143–175.

- Atchley, A. A., & Prosperetti, A. (1989). The crevice model of bubble nucleation. *Journal of the Acoustical Society of America*, 86(3), 1065–1084.
- Berntsen, G. S., Kjeldsen, M., & Arndt, R. E. (2001). Numerical modeling of sheet and tip vortex cavitation with FLUENT 5. In *Fourth International Symposium on Cavitation*. Pasadena, CA.
- Briggs, L. J. (2004). Limiting negative pressure of water. *Journal of Applied Physics*, 21(7), 721–722.
- Chahine, G. L. (2009). Numerical simulation of bubble flow interactions. *Journal of Hydrodynamics, Ser. B*, 21(3), 316–332.
- Chahine, G. L., & Hsiao, C.-T. (2000). Modeling 3D Unsteady Sheet Cavities Using a Coupled UnRANS-BEM Code. In *23rd Symposium on Naval Hydrodynamics*. Val de Reuil, France.
- Chen, Y., & Heister, D. D. (1994). A numerical treatment for attached cavitation. *Journal of Fluids Engineering*, 116, 613–618.
- Choi, J.-K., Hsiao, C.-T., & Chahine, G. L. (2004). Tip Vortex Cavitation Inception Study Using the Surface Averaged Pressure (SAP) Model Combined with a Bubble Splitting Model. In *25th Symposium on Naval Hydrodynamics*. St. John's, NL, Canada.
- Chorin, A. J. (1967). A Numerical Method for Solving Incompressible Viscous Flow Problems. *Journal of Computational Physics*, 2, 12–26.
- Dabiri, S., Sirignano, W. A., & Joseph, D. D. (2007). Cavitation in an orifice flow. *Physics of Fluids*, 19.
- Dabiri, S., Sirignano, W. A., & Joseph, D. D. (2008). Two-Dimensional and axisymmetric viscous flow in apertures. *J. Fluids Mech.*, 605, 149–155.
- Deshpande, M., Feng, J., & Merkle, C. L. (1993). Navier-Stokes Analysis of 2D Cavity Flows. In *Cavitation and Multiphase Flow FED-Vol. 153* (pp. 149–155).
- Fedkiw, R. P., Aslam, T., Merriman, B., & Osher, S. (1999). A non-oscillatory Eulerian approach to interfaces in multimaterial flows (the ghost fluid method). *Journal of Computational Physics*, 169, 463–502.
- Forero, M. (2010). *An investigation on the hydrodynamic impact of treating propeller blade surface to resist cavitation erosion*. NSWCCD-50-TR-2010/023.
- Haberman, W. L., & Morton, R. K. (1953). *An Experimental Investigation of the Drag and Shape of Air Bubble Rising in Various Liquids*. DTMB Report 802.
- Harvey, E. N., Whiteley, A. H., McElroy, W. D., Pease, D. C., & Barnes, D. K. (1944). Bubble formation in animals. II. Gas nuclei and their distribution in blood and tissues. *Journal of Cellular and Comparative Physiology*, 24(1), 23–34.
- Hirschi, R., Dupont, P., & Avellan, F. (1998). Partial sheet cavities prediction on a twisted elliptical platform hydrofoil using a fully 3-D approach. In *3rd international Symposium on Cavitation* (pp. 245–249). Grenoble, France.
- Hsiao, C. T., Ma, J., & Chahine, G. L. (2014). Multi-scale two-phase flow modeling of sheet and cloud cavitation. In *30th Symposium on Naval Hydrodynamics*. Hobart, Tasmania, Australia.
- Hsiao, C.-T., & Chahine, G. L. (2004). Prediction of Vortex Cavitation Inception Using Coupled Spherical and Non-Spherical Models and Navier-Stokes Computations. *Journal of Marine Science and Technology*, 8(3), 99–108.
- Hsiao, C.-T., Chahine, G. L., & Liu, H.-L. (2003). Scaling effect on prediction of cavitation inception in a line vortex flow. *Journal of Fluids Engineering*, 125(1), 53–60.
- Kang, M., Fedkiw, R. P., & Liu, L. . (2000). A Boundary Condition Capturing Method for Multiphase Incompressible Flow. *Journal of Scientific Computing*, 15(3), 323–360.
- Kawamura, T., & Sakoda, M. (2003). Comparison of bubble and sheet cavitation models for simulation of cavitating flow over a hydrofoil. In *Fifth International Symposium on Cavitation*. Osaka, Japan.
- Kinnas, S. A., & Fine, N. E. (1993). A Numerical Nonlinear Analysis of the Flow Around Two- and Three-Dimensional Partially Cavitating Hydrofoils. *J. Fluids Mech.*, 254, 151–181.
- Kinzel, M. P., Lindau, J. W., & Kunz, R. F. (2009). A level-set approach for Large scale cavitation,” DoD High Performance Computing Modernization Program Users Group Conference. In *DoD High Performance Computing Modernization Program Users Group Conference*. San Diego, CA.
- Kunz, R. F., Boger, D. A., Stinebring, D. R., Chyczewski, T. S., Lindau, J. W., & Gibeling, H. J. (2000). A preconditioned Navier-Stokes method for two-phase flows with application to cavitation. *Computers and Fluids*, 29, 849–875.
- Ma, J., Chahine, G. L., & Hsiao, C.-T. (2015). Spherical bubble dynamics in a bubbly medium using an Euler–Lagrange model. *Chemical Engineering Science*, 128, 64–81.
- Merkle, C. L., Feng, J., & Buelow, P. E. O. (1998). Computational modeling of the dynamics of sheet

- cavitation. In *3rd International Symposium on Cavitation (CAV1998)*. Grenoble, France.
- Mørch, K. (2009). Cavitation Nuclei: Experiments and Theory. *Journal of Hydrodynamics, Ser. B*, 21(2), 176–189.
- Osher, S., & Fedkiw, R. P. (2001). Level set methods, an overview and some recent results. *Journal of Computational Physics*, 169, 463–502.
- Roe, P. L. (1981). Approximate Riemann Solvers, Parameter Vectors, and Difference Schemes. *Journal of Computational Physics*, 43, 357–372.
- Rood, E. P. (1991). Review—Mechanisms of Cavitation Inception. *Journal of Fluids Engineering*, 113(2), 163. doi:10.1115/1.2909476
- Saffman, P. G. (1965). The lift on a small sphere in a slow shear flow. *Journal of Fluid Mechanics*, 22(02), 385–400.
- Singhal, N. H., Athavale, A. K., Li, M., & Jiang, Y. (2002). Mathematical basis and validation of the full cavitation model. *Journal of Fluids Engineering*, 124(1-8).
- Sussman, M., Smereka, P., & Osher, S. (1998). An Improved Level Set Approach for Incompressible Two-Phase Flows. *Journal of Computational Physics*, 148, 81–124.
- Van Leer, B., & Woodward, P. R. (1979). The MUSCL Code for Compressible Flow: Philosophy and Results. In *TICOM Conferece*. Austin, TX.
- Vanden, K. J., & Whitfield, D. L. (1995). Direct and Iterative Algorithms for the Three-Dimensional Euler Equations. *AIAA Journal*, 33(5), 851–858.
- Varghese, A. N., Uhlman, J. S., & Kirschner, I. N. (2005). Numerical Analysis of High-Speed Bodies in Partially Cavitating Axisymmetric Flow. *Journal of Fluids Engineering*, 127(1), 41.
- Yount, D. E. (1979). Skin of varying permeability: A stabilization mechanism for gas cavitation nuclei. *The Journal of the Acoustical Society of America*, 65(6), 1429–1439.
- Yuan, W., Sauer, J., & Schnerr, G. H. (2001). Modeling and computation of unsteady cavitation flows in injection nozzles. *Mécanique & Industries*, 2(5), 383–394.